Development and Characterization of Nb3Sn/Al2O3 Superconducting Multilayers for High-performance Radio-Frequency Applications

Chris Sundahl
University of Wisconsin–Madison
Junki Makita
Old Dominion University
Paul Welander
SLAC National Accelerator Laboratory
Yi-Feng Su
Florida State University
Fumitake Kametani
Florida State University
Lin Xie
Southern University of Science and Technology
Huimin Zhang
West Virginia University
Alex Gurevich
Old Dominion University
Chang-Beom Eom (EOM@ENGR.WISC.EDU)
University of Wisconsin–Madison
Lian Li
West Virginia University

Research Article

Keywords: Superconducting radio-frequency (SRF), high-energy particles, magnetic fields, superconductors

Posted Date: January 22nd, 2021

DOI: https://doi.org/10.21203/rs.3.rs-151336/v1

Version of Record: A version of this preprint was published at Scientific Reports on April 8th, 2021. See the published version at https://doi.org/10.1038/s41598-021-87119-9.

Development and characterization of Nb_3Sn/Al_2O_3 superconducting multilayers for high-performance radio-frequency applications

Chris Sundahl[1], Junki Makita[2], Paul B. Welander[3], Yi-Feng Su[4], Fumitake Kametani[4,5], Lin Xie[6], Huimin Zhang[7], Lian Li[7], Alex Gurevich[2]*, Chang-Beom Eom[1]*

Superconducting radio-frequency (SRF) resonator cavities provide extremely high quality factors > 10^{10} at 1-2 GHz and 2K in large linear accelerators of high-energy particles. The maximum accelerating field of SRF cavities is limited by penetration of vortices into the superconductor. Present state-of-the-art Nb cavities can withstand up to 50 MV/m accelerating gradients and magnetic fields of 200-240 mT which destroy the low-dissipative Meissner state. Achieving higher accelerating gradients requires superconductors with higher thermodynamic critical fields, of which Nb_3Sn has emerged as a leading material for the next generation accelerators. To overcome the problem of low vortex penetration field in Nb_3Sn, it has been proposed to coat Nb cavities with thin film Nb_3Sn multilayers with dielectric interlayers. Here, we report the growth and multi-technique characterization of stoichiometric Nb_3Sn/Al_2O_3 multilayers with good superconducting and RF properties. We developed an adsorption-controlled growth process by co-sputtering Nb and Sn at high temperatures with a high overpressure of Sn. The cross-sectional scanning electron transmission microscope images show no interdiffusion between Al_2O_3 and Nb_3Sn. Low-field RF measurements suggest that our multilayers have quality factor comparable with cavity-grade Nb at 4.2 K. These results provide a materials platform for the development and optimization of high-performance SIS multilayers which could overcome the intrinsic limits of the Nb cavity technology.

[1]Department of Materials Science and Engineering, University of Wisconsin-Madison, Madison, WI 53706. [2]Physics Department and Center for Accelerator Science, Old Dominion University, Norfolk, VA 23529. [3]SLAC National Accelerator Laboratory, Menlo Park, CA 94025. [4]Applied Superconductivity Center, National High Magnetic Field Laboratory, Florida State University. [5]Department of Mechanical Engineering, FAMU-FSU College of Engineering, Tallahassee, FL 32310. [6]Department of Physics, Southern University of Science and Technology, Shenzhen, 518055, China. [7]Department of Physics and Astronomy, West Virginia University, Morgantown, WV 26506.

*eom@engr.wisc.edu, agurevic@odu.edu

Introduction

For decades, Nb has been the material of choice for the radio-frequency superconducting (SRF) resonators for high-energy particle accelerators. Technological advances have resulted in the development of Nb cavities which can exhibit extremely high quality factors $Q > 10^{10}$ @ 1-2 GHz and 2 K while sustaining accelerating gradients up to 50 MV/m [1–3]. Such exemplary performance and low RF losses can only be achieved if the cavities operate in a Meissner state which can persist up to the maximum magnetic field at the inner cavity surface reaches the superheating field B_s = 240 mT [1–3]. At $B = B_s$ the low-dissipative Meissner state becomes absolutely unstable with respect to dissipative penetration of vortices, causing an explosive increase of RF power and thermal quench of the cavity. The state-of-the-art Nb cavities can already operate at the peak magnetic field close to B_s, thus, increasing accelerating gradients beyond the intrinsic limits of Nb requires materials with higher B_s. There are many such materials but all of them are type-II superconductors with lower critical field B_{c1} smaller than $B_{c1} \approx 170 - 180$ mT of Nb which makes high-B_s superconductors prone to detrimental penetration of vortices at low fields[4,5]. To overcome this problem, it was proposed to nanostructure the inner surface of Nb cavities by coating it with multilayers of thin superconductors (S) separated by dielectric insulating (I) layers (

Figure ***1***)[6]. Here the S-layer material has a superheating field B_s higher than B_{s0} of Nb, whereas the thickness d of S layers is smaller than the London penetration depth λ, and the thickness of I layers can be a few nm to suppress the interlayer Josephson coupling. Such SIS structures greatly increase barriers for penetration of vortices in the bulk of the cavity which could potentially withstand the RF fields limited by the superheating field of S-layer. For instance, using Nb_3Sn with $B_s = 480$ mT could nearly double the maximum accelerating gradient as compared to the best Nb cavities. The multilayer approach is based on the lack of thermodynamically stable parallel vortices in thin decoupled S screens at $B < B_{c1}$ where B_{c1} is strongly enhanced in films with $d < \lambda$ [6–10]. Because the inner surface of the Nb cavity is partially screened by multilayers, both Q(H) and the breakdown field can be increased due to lower surface resistance R_s and higher H_c of the layer material[6].

The multilayer coating, which opens up a principal opportunity to break the Nb monopoly in SRF cavities, has been tested by several groups using MgB_2, Nb_3Sn, NbN, NbTiN, and dirty Nb as coating materials. These experiments have shown an increase of the dc field onset of penetration of vortices on Nb surfaces coated with different SIS structures[4,11–19], although such key SRF characteristics as the surface resistance and quality factors of SIS multilayers under high-amplitude RF fields have been investigated to a much lesser extent. The first results on low-field Q measurements on NbN/MgO multilayers [13,19] have shown that SIS multilayers can have lower R_s than bulk Nb. However, the SRF performance of Nb_3Sn, the current material of choice for the next generation coating material[20], has not yet been investigated in SIS structures. The development of SIS structures requires overcoming many materials science and technological challenges to achieve good superconducting properties are SRF performance while providing optimal stoichiometry and morphology of the layers and the interfaces and transparency of grain

boundaries to extremely high RF current densities. In this work we report results on growth and characterizations of Nb_3Sn/Al_2O_3 multilayers which exhibit good superconducting properties and low-field SRF performance on par with the cavity-grade Nb.

Results and discussion

Multilayer growth We developed a technique of high-temperature confocal sputtering of Nb and Sn from elemental targets to grow stoichiometric Nb_3Sn multilayers with Al_2O_3 interlayers. Details are given in the Supplemental Information. Thin films and multilayers of different thicknesses were grown on different sapphire single crystal substrates for the subsequent characterizations. For instance, 60 nm thick Nb_3Sn films were grown on 10 x 10 mm sapphire substrates for transport, scanning tunneling spectroscopy and electron microscopy characterizations. For RF tests, we grew Nb_3Sn/Al_2O_3 multilayers on 2" diameter sapphire wafers (R-plane, 300 μm thick). These multilayers had up to three 60 nm Nb_3Sn layers separated by 6 nm Al_2O_3. The thickness of the Nb_3Sn layers was chosen to be smaller than the London penetration depth [5,6]. A 200 nm thick Nb film was deposited on the backside of the wafers to prevent leakage of RF field during cavity measurements. The geometry of multilayer samples used in our RF measurements of quality factors is shown in Figure 1.

The Nb-Sn phase diagram contains several line compounds. For instance, Nb_3Sn and Nb_6Sn_5 coexist in the region marked in Figure 2a. Here a low-T_c Nb_6Sn_5 phase is clearly undesirable in these films [21]. Within the Nb_3Sn phase region extending from 17-25 % Sn, the critical temperature T_c degrades steeply as stoichiometry moves away from a 3:1 ratio [22]. These two conditions demand that Nb_3Sn films should contain 25% of Sn. This was accomplished by providing processing conditions reflecting the field in the upper right of the phase diagram in Figure 2a, a two-phase region containing only stoichiometric Nb_3Sn and liquid Sn. Films were grown by confocal sputtering of Nb and Sn from elemental targets. By providing a large over-pressure of Sn at high growth temperatures, it has been found that the ratio of Nb:Sn can be pinned at 3:1. The abundance of Sn drives the material into the two-phase region, where excess Sn re-evaporates from the film, avoiding the formation of Sn precipitates[23,24]. To achieve the high temperatures (>930 °C) required for this growth, sapphire substrates were heated from behind with a SiC radiative heater. Radiation passed through the substrate and heated the depositing metal directly. Growth temperature was measured by pyrometer. Details of the film growth are given in the Supplemental information.

A series of films was grown with fixed Nb flux (0.7 Å/s) and varying Sn flux (0.4-2.5 Å/s), and low-temperature resistance measurements were carried out to find the window for this self-regulating adsorption-controlled process. Shown in Figure 2b are the dependencies of the critical temperature T_c and transition width ΔT_c on the deposition rate of Sn which clearly saturate at ~1 Å/s. Given the dependence of T_c on Sn content in Nb_3Sn, this growth rate roughly corresponds to the boundary between two processing regimes. At lower flux, Sn that is necessary to form stoichiometric Nb_3Sn evaporates before it can be incorporated into the film. At higher flux, the sufficient Sn is provided to react with all available Nb, and excess Sn re-evaporates.

The dielectric Al_2O_3 interlayers were grown after allowing Nb_3Sn to cool down to <400 °C, using a single stoichiometric target with RF power at a rate of 1.8 nm/min without any further heating applied to the substrate. Depositing under these conditions protects the SiC heater element from oxygen evolved during the sputtering process and prevents undesired reactions with the Nb_3Sn surface. This Nb_3Sn/Al_2O_3 stack was then heated again to 900+ °C, which allows the Al_2O_3 to crystallize, and the process was repeated to grow heterostructures of up to three Nb_3Sn layers. The chamber setup and growth steps are depicted in

Figure ***3***.

Structural characterization A SIS sample with three Nb_3Sn layers was prepared for analysis by cross-sectional scanning transmission electron microscopy (STEM). A low-magnification image (

Figure ***4***a) represents the morphology and nanostructure of the stack. Each Nb_3Sn layer is polycrystalline with irregular interfaces and grain size is 20-100 nm along the film surface direction. The Al_2O_3 layers conform closely to the layer below but are discontinuous along the Nb_3Sn/Al_2O_3 interface. Despite the repeated thermal cycling during stacking, it appears that the lower layers have not degraded in comparison to the top layer.

The chemical stability of these films is further confirmed by compositional mapping with energy dispersive spectroscopy (EDS) (

Figure ***4***b). Intensity of the Al Kα and O Kα peaks are mapped from the region shown on the left. Although the Al_2O_3 layers are not continuous, Al and O are confined to the Al_2O_3 layers, and do not mix with the Nb_3Sn layers. The exception to this is the presence of O at the interface of the topmost Nb_3Sn film with the atmosphere, where ambient conditions are sufficient to cause a reaction. Note that the slight O signal in the Nb_3Sn layers in Figure 4b are due to the slight oxidation of the TEM specimen surface. As our RF cavity measurements show, these Al_2O_3 layers do not contribute significantly to surface resistance at low fields.

A higher-magnification image of the S-I interface is shown in

Figure ***4***c. The atomic structure of Nb_3Sn is well-preserved at the interface, suggesting that there is almost no diffusion or intermixing from the Al_2O_3. The lower Nb_3Sn grain orients the [023] direction normal to the film surface, and this direction is also preserved in the upper Nb_3Sn grain. This can occur when the upper Nb_3Sn layer deposits with the same epitaxial relationship to the underlying Al_2O_3 as the lower layer has with the Al_2O_3 substrate. This structure can also form when a Nb_3Sn grain nucleates on top of a Nb_3Sn surface exposed by breaks in the discontinuous Al_2O_3 layer. X-ray diffractometry indicates that Nb_3Sn grains in the second layer have more random crystallographic orientation compared to the first layer (see the Supplemental material).

Superconducting properties. Our dc transport measurements have shown that the Nb_3Sn films capped with Al_2O_3 and annealed with no further deposition exhibit good superconducting

properties. For instance, the superconducting resistive transitions of a bare Nb_3Sn film and a Nb_3Sn/Al_2O_3 structure annealed at 900 °C for 10 minutes are shown in

Figure *5*a. Here the critical temperature of the annealed sample is about 0.25 K higher than T_c of the unannealed sample, and residual resistivity ratio (RRR), an indicator of crystalline and metallic quality, is improved from 3.5 to 4.26. On the other hand, Nb_3Sn films annealed *without* the Al_2O_3 cap, even under high Sn flux to prevent evaporative loss, have degraded superconducting properties compared to an un-annealed film.

The superconducting properties essential for the RF performance were characterized by the scanning tunneling spectroscopy (STS) which measures the differential tunneling conductance dI/dV proportional to the quasiparticle density of states (DOS), N(E). Shown in

Figure *5*b is a representative tunneling spectrum measured in the center of a Nb_3Sn grain at 4 K. The DOS curves, which clearly show the superconducting gap Δ at the Fermi surface, were fit using the conventional Dynes model [25,26]:

$$N(E) = N_0 Re\left[\frac{E - i\Gamma}{\sqrt{(E - i\Gamma)^2 - \Delta^2}}\right] \qquad (1)$$

where the phenomenological parameter Γ accounts for the broadening of the DOS peaks due to a finite lifetime of quasiparticles, and N_0 is the DOS in the normal state. The fit was done with Γ = 0.4 meV and $\Delta \approx 3.1$ meV, consistent with the conventional gap value for a stoichiometric Nb_3Sn [4]. The ratio $\Gamma/\Delta \approx 13$ % in our samples turns out to be about 2-3 times larger than the values observed by tunneling spectroscopy on 1-2 μm thick Nb_3Sn films for rf applications[27] and Nb coupons[28]. The deviations of the STM data from the Dynes model at low energies $E < \Delta$ may indicate the effects of local non-stoichiometry, gap anisotropy and strain [22], scattering of quasiparticles on magnetic impurities, and a thin layer with deteriorated superconducting properties at the surface [27,28,29,30]. In turn, the subgap quasiparticles states which appear at |E| < Δ due to a finite Γ contribute to a temperature-independent residual surface resistance R_i at k_BT << Δ [5,29]

$$R_i = \frac{\mu_0^2 \omega^2 \lambda^3 \Gamma^2}{2\rho_n(\Delta^2 + \Gamma^2)} \qquad (2)$$

Here μ_0 is the permeability of free space, ρ_n is the normal-state resistivity, λ is the magnetic penetration depth, and $\omega = 2\pi f$ is the circular RF frequency [5]. For λ = 120 nm, $\rho_n = 3.0 \times 10^{-7}$ Ωm, and the fit parameters Δ = 3.1 meV and Γ = 0.4 meV, we obtain $R_i \approx 5.0$ nΩ at f = 1.3 GHz. This estimate is of the order of $R_i \approx$ 5-10 nΩ for large-grain Nb cavities [31]. Below a few nm thick surface layer but well within the rf penetration depth λ ≈ 120 nm, the gap peaks in the DOS are likely much sharper. There are other essential contributions to R_i most notably due to non-stoichiometric regions in the bulk[27], grain boundaries and trapped vortices [32].

Low-field RF characterization Multilayer samples grown on 2" sapphire wafers were tested in a hemispherical Nb-coated cavity at SLAC National Accelerator Laboratory. The experimental setup was described previously [33]. A rendering of this cavity is shown in Figure 6b**Error! Reference source not found.**. The cavity operates in a TE_{032}-like mode at 11.4 GHz, with a pocket on the flat face for mounting 2"-diameter samples (shown in purple). The overall cavity quality factor is measured, and the properties of the wafer can be deduced by comparison with known samples. The geometry of the cavity is engineered such that the magnetic field is strongest at the sample surface, limiting the contribution of the cavity material to the overall cavity loss. According to simulations, the participation factor is 0.33 for the 2"-diameter sample. Crucially, the magnetic field at the sample is in the radial direction and parallel to the sample surface, making it possible to measure RF properties of the sample without interference from the perpendicular component of the field.

The SRF performance of two Nb_3Sn samples were compared in this system to a cavity-grade bulk Nb coupon. A 500 nm (~4λ) Nb_3Sn film intended to completely screen out the RF magnetic field, and a 3x60 nm Nb_3Sn/Al_2O_3 trilayer were tested under the RF field. Both samples were coated with a 200 nm Nb film on the backside of the wafer to prevent leakage of magnetic field as shown in Figure 1. The quality factor of the cavity with each sample, measured at low power with a network analyzer, is plotted in Figure 6a. The abrupt increase in Q at about 15 K corresponds to the superconducting transition of Nb_3Sn, followed by an increase of Q(T) at T_c = 9K of the Nb-coated host cavity.

As shown in

Figure ***6***a, the thick Nb_3Sn film and the trilayer have nearly identical Q at T < 9K, indicating that Al_2O_3 dielectric layers and interfaces do not contribute significantly to the RF dissipation. We would expect the thick Nb_3Sn film to have a higher Q, as magnetic field is more fully screened before reaching the substrate and backside, so this result suggests that the maximum Q of these films and multilayers is limited by the quality of the Nb_3Sn material rather than by the interfaces with Al_2O_3. The quality factors of both the film and the trilayer samples exceed Q(T) of Nb at T > 6K due to the higher T_c of Nb_3Sn and is about 2 times smaller than Q of Nb at 4K.

Discussion The results of this work show that, despite the obvious non-stoichiometry and inhomogeneity of superconducting properties, grain boundaries, Nb inclusions, and incomplete Al_2O_3 layers, our multilayers exhibit the quality factors on par of those of cavity-grade bulk Nb at 4K and low RF power. The significant local non-stoichiometry of thick (a few micron) polycrystalline Nb_3Sn coatings of Nb cavities [20,27] , as well as Sn depletion at grain boundaries in Nb_3Sn [34–37] have been well documented in the literature. Yet, despite these materials issues which are also characteristic of 1-3 μm thick Nb_3Sn films used in SRF cavities [38], our Nb_3Sn SIS structures exhibit higher low-field Q values than Nb at T > 6K [20], consistent with the larger superconducting energy gap $\Delta_{Nb3Sn} \approx 2\Delta_{Nb}$ and a lower BCS surface resistance $R_{BCS} \propto \omega^2 \rho_n^{1/2} e^{-\Delta/k_B T}$ of Nb_3Sn. These experimental results not only show a remarkable resilience of

low-field quality factors of Nb_3Sn to the significant non-stoichiometry and materials imperfections but also suggest that the SRF performance of Nb_3Sn coatings can be further improved by materials treatments. Our Nb_3Sn multilayers exhibit a similar resilience of the low-power SRF performance to the materials imperfections.

The slopes of Q(T) for both the Nb_3Sn film and multilayer shown in Fig. 5 tend to level off at 4-5 K and are clearly smaller than the slope of Q(T) for Nb. This indicates that Q(T) of the Nb_3Sn samples at T = 4 - 5 K is not limited by the BCS surface resistance for which the slope of $Q(T) \propto e^{\Delta/k_BT}$ for Nb_3Sn would be larger than for Nb because $\Delta_{Nb3Sn} \approx 2\Delta_{Nb}$. The behavior of Q(T) of the Nb_3Sn samples at 4-5 K is thus indicative of a significant residual surface resistance caused by the multiphase structure of the films and multilayers and trapped vortices. Yet $Q_0 \simeq 10^7$ observed on our Nb_3Sn multilayers at 11.4 GHz and 4 K suggests values of $Q_0 \sim 10^9$ at 4K and 1 GHz given the frequency dependence $Q \propto \omega^{-2}$ which comes from the BCS surface resistance [1–3], ohmic losses in metallic precipitates smaller than the RF skin depth and perhaps Josephson vortices trapped on grain boundaries [39].

SRF performance at high RF fields and breakdown fields of Nb_3Sn/Al_2O_3 multilayers are yet to be explored. Generally, the effects of nonstoichiometry, proximity-coupled normal precipitates and weakly-coupled grain boundaries become more pronounced at higher RF fields. For instance, nonstoichiometric grain boundaries in Nb_3Sn have been identified as prime pinning centers for vortices in Nb_3Sn wires for high-field dc magnets [39]. However, weakly-coupled grain boundaries in Nb_3Sn coating layers would block RF currents and cause dissipative penetration of Josephson vortices at fields well below the superheating field [40], and sub-stoichiometric regions in Nb_3Sn-coated Nb cavities are suspected to play an important role in RF cavity quench [27] . At the same time, significant meandering and breaks in Al_2O_3 layers shown in Figure 4 may not be detrimental for SRF performance as the layers can still provide their main role of intercepting and pinning small vortex loops originating at surface structural defects [5,8] since the pinholes sizes 10-50 nm in the Al_2O_3 layers are smaller than magnetic size of the vortex $\lambda \simeq 100 - 200$ nm of Nb_3Sn. Though Al_2O_3 layers do not fully separate Nb_3Sn layers, we found that a 500 nm thick Nb_3Sn film had a quality factor identical to a multilayer with three 60 nm Nb_3Sn layers separated by 6 nm Al_2O_3, and both had Q approximately 2x lower than a cavity-grade Nb reference. This is strong evidence that the Al_2O_3 and the oxide-metallic interfaces do not contribute to surface resistance samples prepared with this process.

Conclusions

In summary, we have developed a self-regulating, adsorption-controlled process for growth of Nb_3Sn films and Nb_3Sn/Al_2O_3 multilayers. We have produced and characterized multiple multilayer samples with up to four superconducting layers. Despite the detrimental effects of nonstoichiometry, grain boundaries and breaks in the meandering Al_2O_3 interlayers, the SRF performance of our multilayers turned out to be on par with that of Nb films. The growth technique

reported in this work provides a platform for further optimizations of the SRF properties of SIS high-performance multilayers for superconducting resonator applications.

Methods

Nb_3Sn films were sputtered from elemental Nb (99.95%) and Sn (99.99%) targets in 3 mTorr of Ar at a distance of 15.5 cm from the substrate. DC power to the sputter guns was current-controlled, and deposition rate was measured with an *in situ* quartz crystal monitor prior to growth. Pyrometer reading of the SiC heating element at the beginning of growth was ~1250 °C, and dropped to around 905 °C after 60 nm was deposited. Al_2O_3 was sputtered from a stoichiometric 2" diameter ceramic target after the pyrometer reading fell below 400 °C. After deposition, the temperature was ramped back up to a pyrometer reading of 905 °C over the course of 10 minutes. These two steps were repeated to produce the multilayers.

Scanning transmission electron microscope (STEM) imaging and elemental analysis were performed in a probe-corrected JEOL JEM-ARM200cF with an Oxford X-Max^N 100TLE SDD energy dispersive X-ray spectroscopy (EDS) detector.

Superconducting transitions were measured in a closed-loop He cooler using 4-point van der Pauw geometry on 10x10 mm samples. The critical temperature T_c is defined as the temperature at which the sheet resistance falls below 1% of its normal state value at 18 K. The transition width ΔT_c is defined as a difference between T_c and the point at which the lines drawn through the normal-state resistance and transition region intersect.

Low-temperature scanning tunneling microscopy/spectroscopy (STM/S) measurements were carried out in a Unisoku-1300 STM system at 4K using polycrystalline PtIr tips. The dI/dV spectra were acquired using standard lock-in technique by applying a bias modulation of 0.2 mV (r.m.s.) at 732 Hz.

Acknowledgement

This work was supported by the US Department of Energy under grant # DE-SC0010081-020. Work at West Virginia University was supported by the U.S. Department of Energy under Award # DE-SC0017632. Work at SLAC National Accelerator Laboratory was supported by the U.S. Department of Energy under contract # DE-AC02-76SF00515. The nanostructural characterizations were supported by the National High Magnetic Field Laboratory and the National Science Foundation under grant # NSF/DMR-1644779), and by the State of Florida.

Author contributions

C.S. developed multilayer growth process and fabricated samples. J.M. participated in RF characterization. Y.S., F.K., and L.X. performed cross-sectional TEM characterization. H.Z. and L.L. performed low-temperature STM characterization. P.B.W. performed low-temperature RF

surface resistance characterization. C.B.E and A.G. initiated and directed the project. C.S and A.G. wrote the manuscript with contributions from all authors.

Competing interests

The authors declare no competing interests.

Data availability

The data that supports the findings of the work are in the manuscripts main text and Supplementary Information. Additional data are available from the corresponding author upon reasonable request.

References

1. Padamsee, H., Knobloch, J. & Hays, T. *RF Superconductivity for Accelerators*. (Wiley New York, 2008).

2. Gurevich, A. Superconducting Radio-Frequency Fundamentals for Particle Accelerators. *Rev. Accel. Sci. Technol.* **05,** 119–146 (2012).

3. Padamsee, H. S. Superconducting Radio-Frequency Cavities. *Annu. Rev. Nucl. Part. Sci.* **64,** 175–196 (2014).

4. Valente-Feliciano, A.-M. Superconducting RF materials other than bulk niobium: a review. *Supercond. Sci. Technol.* **29,** 113002 (2016).

5. Gurevich, A. Theory of RF superconductivity for resonant cavities. *Supercond. Sci. Technol.* **30,** 034004 (2017).

6. Gurevich, a. Enhancement of rf breakdown field of superconductors by multilayer coating. *Appl. Phys. Lett.* **88,** 012511 (2006).

7. Kubo, T., Iwashita, Y. & Saeki, T. Radio-frequency electromagnetic field and vortex penetration in multilayered superconductors. *Appl. Phys. Lett.* **104,** 032603 (2014).

8. Gurevich, A. Maximum screening fields of superconducting multilayer structures. *AIP Adv.* **5,** 017112 (2015).

9. Liarte, D. B. *et al.* Theoretical estimates of maximum fields in superconducting resonant radio frequency cavities: stability theory, disorder, and laminates. *Supercond. Sci. Technol.* **30,** 033002 (2017).

10. Kubo, T. Multilayer coating for higher accelerating fields in superconducting radio-frequency cavities: a review of theoretical aspects. *Supercond. Sci. Technol.* **30,** 023001 (2017).

11. Antoine, C. Z. *et al.* Characterization of superconducting nanometric multilayer samples for superconducting rf applications: First evidence of magnetic screening effect. *Phys. Rev. Spec. Top. - Accel. Beams* **13,** 121001 (2010).

12. Tajima, T. *et al.* Studies on thin film MgB_2 for applications to RF structures for particle accelerators. in *AIP Conference Proceedings* **1435,** 297–304 (2012).

13. Antoine, C. Z., Villegier, J.-C. & Martinet, G. Study of nanometric superconducting multilayers for RF field screening applications. *Appl. Phys. Lett.* **102,** 102603 (2013).

14. Beringer, D. B. *et al.* Thickness Dependence and Enhancement of H_{c1} in Epitaxial MgB_2 Thin Films. *IEEE Trans. Appl. Supercond.* **23,** 7500604–7500604 (2013).

15. Roach, W. M., Beringer, D. B., Li, Z., Clavero, C. & Lukaszew, R. A. Magnetic Shielding Larger Than the Lower Critical Field of Niobium in Multilayers. *IEEE Trans. Appl. Supercond.* **23,** 8600203–8600203 (2013).

16. Tan, T. *et al.* Enhancement of lower critical field by reducing the thickness of epitaxial and polycrystalline MgB_2 thin films. *APL Mater.* **3,** 041101 (2015).

17. Tan, T., Wolak, M. A., Xi, X. X., Tajima, T. & Civale, L. Magnesium diboride coated bulk niobium: a new approach to higher acceleration gradient. *Sci. Rep.* **6,** 35879 (2016).

18. Junginger, T., Wasserman, W. & Laxdal, R. E. Superheating in coated niobium. *Supercond. Sci. Technol.* **30,** 125012 (2017).

19. Antoine, C. Z. *et al.* Optimization of tailored multilayer superconductors for RF application and protection against premature vortex penetration. *Supercond. Sci. Technol.* **32,** 085005 (2019).

20. Posen, S. & Hall, D. L. Nb_3Sn superconducting radiofrequency cavities: fabrication, results, properties, and prospects. *Supercond. Sci. Technol.* **30,** 033004 (2017).

21. Charlesworth, J. P., Macphail, I. & Madsen, P. E. Experimental work on the niobium-tin constitution diagram and related studies. *J. Mater. Sci.* **5,** 580–603 (1970).

22. Godeke, A. A review of the properties of Nb_3Sn and their variation with A15 composition, morphology and strain state. *Supercond. Sci. Technol.* **19,** R68–R80 (2006).

23. Allen, L. H., Anklam, W., Beasley, M. R., Hammond, R. H. & Turneaure, J. P. RF surface resistance in Nb_3Sn thin films. *IEEE Trans. Magn.* **21,** 525–527 (1985).

24. Allen, L.H., Beasley, M.R., Hammond, R.H., Turneaure, J.P. RF Surface Resistance of Nb_3Sn, NbZr, and NbN Thin Films. *IEEE Trans. Magn.* **23,** 1405–1408 (1987).

25. Dynes, R. C., Narayanamurti, V. & Garno, J. P. Direct Measurement of Quasiparticle-Lifetime Broadening in a Strong-Coupled Superconductor. *Phys. Rev. Lett.* **41,** 1509–1512 (1978).

26. Dynes, R. C., Garno, J. P., Hertel, G. B. & Orlando, T. P. Tunneling Study of Superconductivity near the Metal-Insulator Transition. *Phys. Rev. Lett.* **53,** 2437–2440 (1984).

27. Becker, C. *et al.* Analysis of Nb_3Sn surface layers for superconducting radio frequency cavity applications. *Appl. Phys. Lett.* **106,** 082602 (2015).

28. Lechner, E. M. *et al.* Electron Tunneling and X-Ray Photoelectron Spectroscopy Studies of the Superconducting Properties of Nitrogen-Doped Niobium Resonator Cavities. *Phys. Rev. Appl.* **13,** 044044 (2020).

29. Gurevich, A. & Kubo, T. Surface impedance and optimum surface resistance of a superconductor with an imperfect surface. *Phys. Rev. B* **96,** 184515 (2017).

30. Proslier, T. *et al.* Tunneling study of cavity grade Nb: Possible magnetic scattering at the surface. *Appl. Phys. Lett.* **92,** 212505 (2008).

31. Visentin, B., Barthe, M. F., Moineau, V. & Desgardin, P. Involvement of hydrogen-vacancy complexes in the baking effect of niobium cavities. *Phys. Rev. Spec. Top. - Accel. Beams* **13,** 052002 (2010).

32. Dhakal, P., Ciovati, G. & Gurevich, A. Flux expulsion in niobium superconducting radio-frequency cavities of different purity and essential contributions to the flux sensitivity. *Phys. Rev. Accel. Beams* **23,** 023102 (2020).

33. Welander, P., Franzi, M. & Tantawi, S. Cryogenic RF characterization of superconducting materials at SLAC with hemispherical cavities. in *Proceedings of SRF2015* 735–738 (2015).

34. Suenaga, M. & Jansen, W. Chemical compositions at and near the grain boundaries in bronze-processed superconducting Nb_3Sn. *Appl. Phys. Lett.* **43,** 791–793 (1983).

35. Sandim, M. J. R. *et al.* Grain boundary segregation in a bronze-route Nb_3Sn superconducting wire studied by atom probe tomography. *Supercond. Sci. Technol.* **26,** 055008 (2013).

36. Lee, J. *et al.* Atomic-scale analyses of Nb_3Sn on Nb prepared by vapor diffusion for superconducting radiofrequency cavity applications: a correlative study. *Supercond. Sci. Technol.* **32,** 024001 (2019).

37. Lee, J. *et al.* Grain-boundary structure and segregation in Nb_3Sn coatings on Nb for high-performance superconducting radiofrequency cavity applications. *Acta Mater.* **188,** 155–165 (2020).

38. Spina, T., Tennis, B. M., Lee, J., Seidman, D. N. & Posen, S. Development and Understanding of Nb_3Sn films for radiofrequency applications through a sample-host 9-cell cavity. *Supercond. Sci. Technol.* **34,** 015008 (2021).

39. Scanlan, R. M., Fietz, W. A. & Koch, E. F. Flux pinning centers in superconducting Nb_3Sn. *J. Appl. Phys.* **46,** 2244–2249 (1975).

40. Sheikhzada, A. & Gurevich, A. Dynamic transition of vortices into phase slips and generation of vortex-antivortex pairs in thin film Josephson junctions under dc and ac currents. *Phys. Rev. B* **95,** 214507 (2017).

Figures Captions

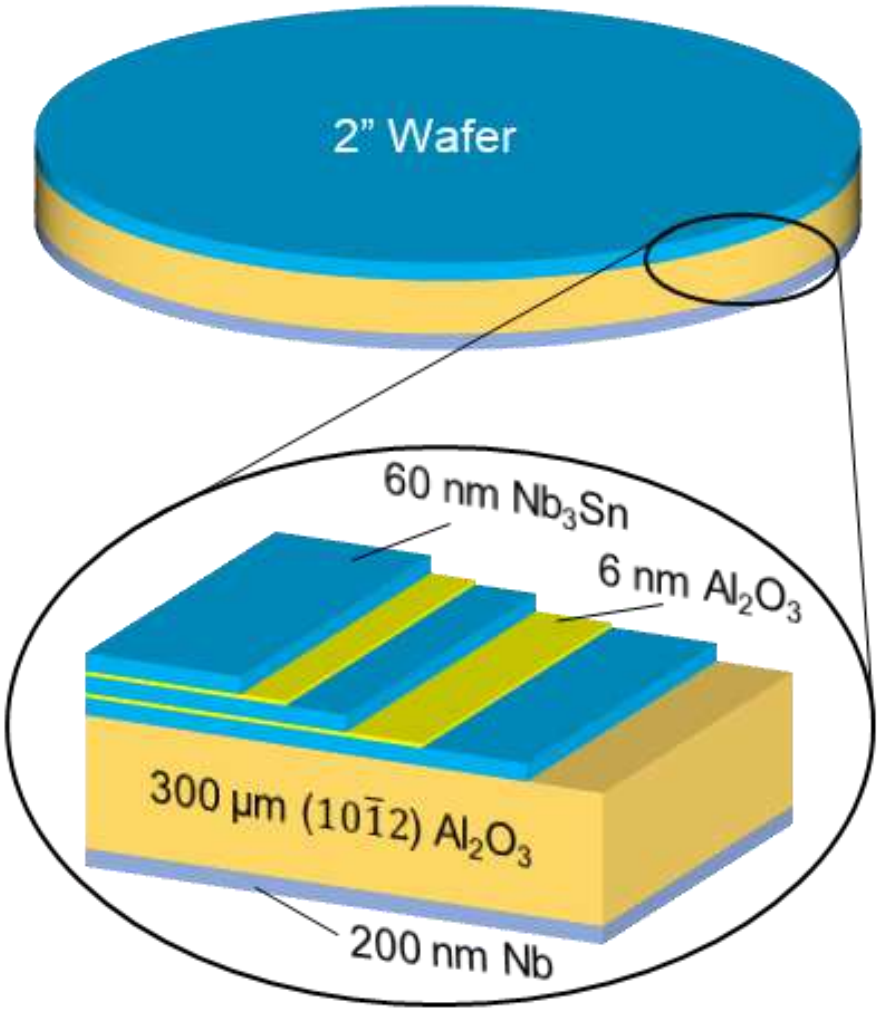

Figure 1. Schematic of Nb_3Sn/Al_2O_3 multilayer heterostructures on Al_2O_3 wafer. Back side of Al_2O_3 wafer is coated with a thick Nb film.

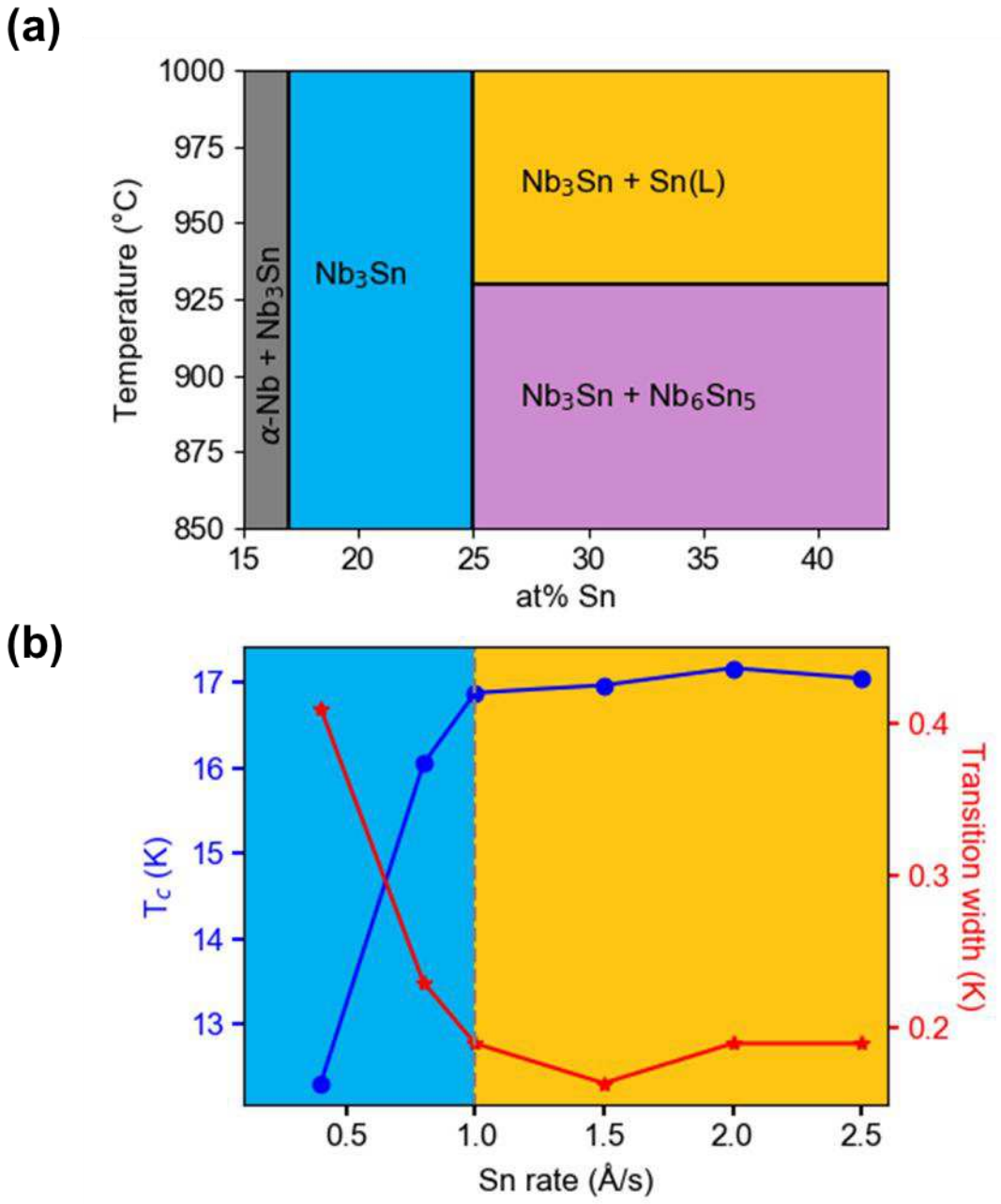

Figure 2. Connecting the Nb-Sn phase diagram to electrical properties and process window. (a) Relevant adsorption-controlled growth regime (orange) of Nb-Sn phase diagram. Nb_3Sn spans 17-25 % Sn, and the desired Nb_3Sn + liquid Sn field lies above 930 °C and 25% Sn. (b) T_c, ΔT_c, vs the Sn flux of 60 nm thick Nb_3Sn single layer thin films on Al_2O_3 substrates. T_c levels off above 1.0 Å/s Sn, corresponding to the adsorption-controlled growth window and the film composition reach 25% Sn.

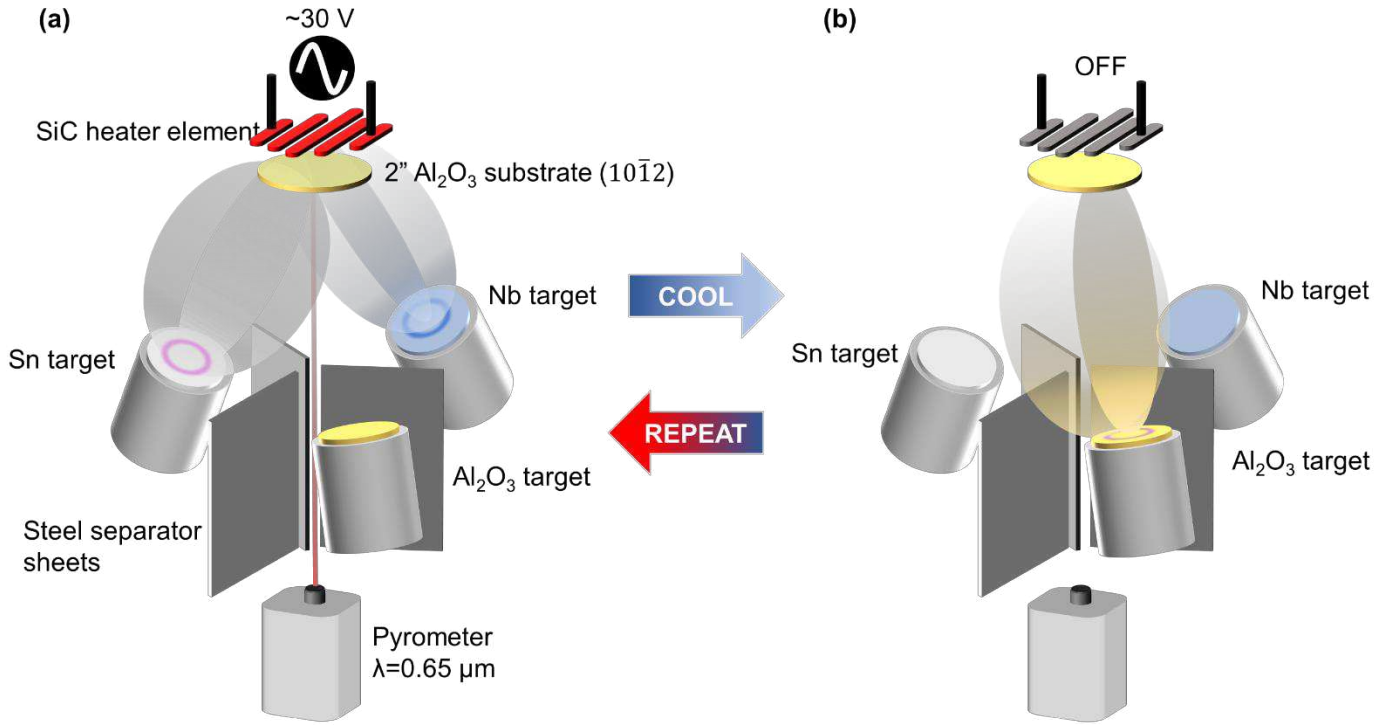

Figure 3. Schematic of thin films deposition setup and sequential processing steps for Nb_3Sn/Al_2O_3 multilayer heterostructures. (a) Nb and Sn are sputtered onto Al_2O_3 substrate while heater element is powered on. (b) After allowing film to cool, Al_2O_3 is sputtered from a single stoichiometric Al_2O_3 target. Sample is heated again to anneal Al_2O_3. These two steps are repeated to produce multilayer samples.

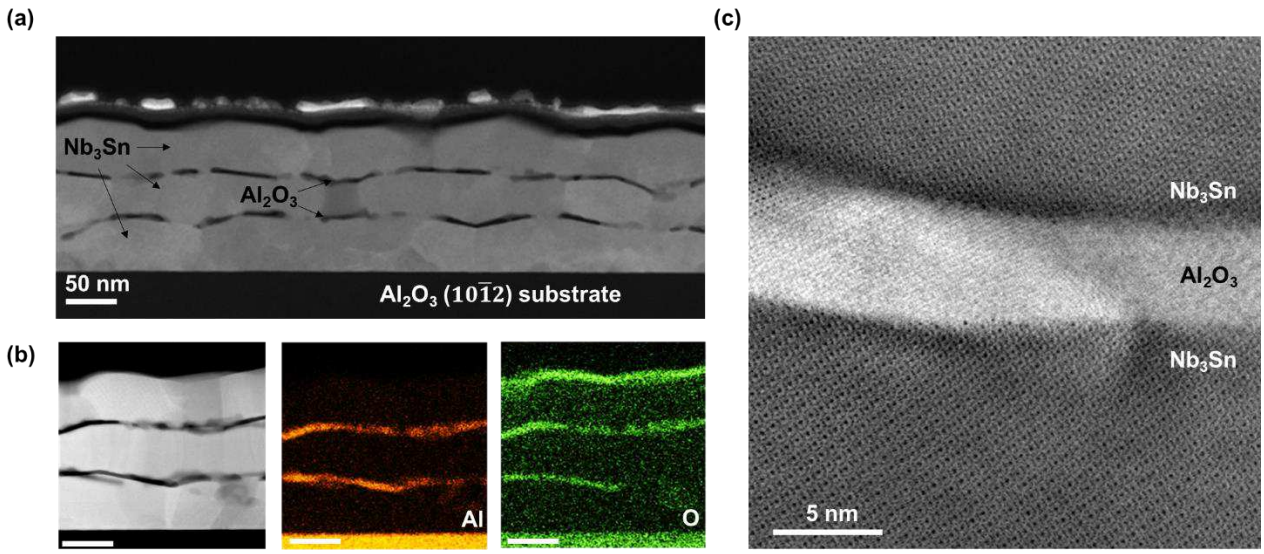

Figure 4. Cross-sectional transmission electron microscopy images of Nb_3Sn/Al_2O_3 multilayer heterostructures (a) Low-magnification image of trilayer morphology. (b) EDS compositional mapping of Al and O showing no interdiffusion between Al_2O_3 and Nb_3Sn. (c) High-magnification image of the interfaces between Al_2O_3 and Nb_3Sn.

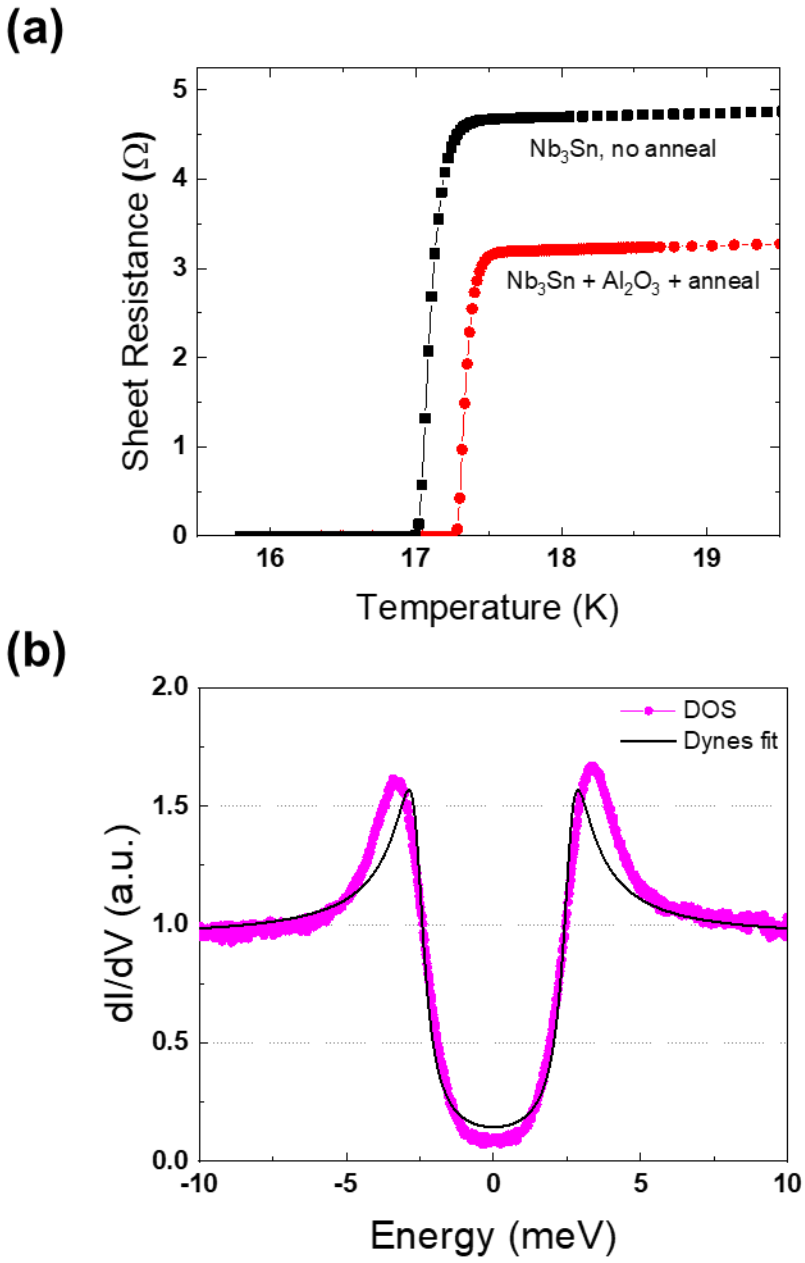

Figure 5. Electrical properties of single-layer Nb_3Sn films. (a) Resistive superconducting transition for two identical 60 nm thick films, one of which is capped with 6 nm Al_2O_3 overlayer and annealed at 900 °C for 10 minutes. (b) Density of states measured by scanning tunneling microscopy and Dynes fit for a 60 nm thick Nb_3Sn film.

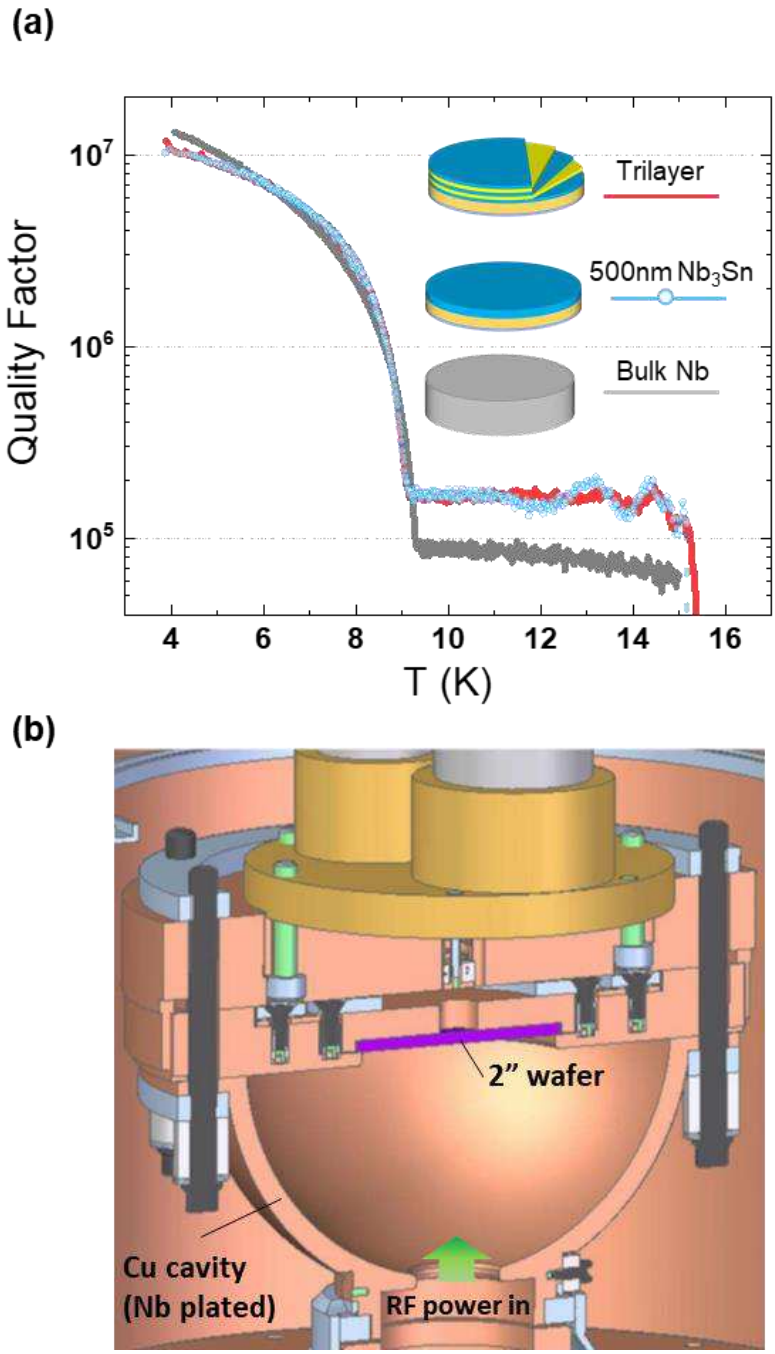

Figure 6. (a) RF Surface resistance measurements of Nb_3Sn film and multilayer compared to cavity-grade Nb. (b) Cutaway of hemispherical resonator cavity at SLAC used for these measurements.

Figures

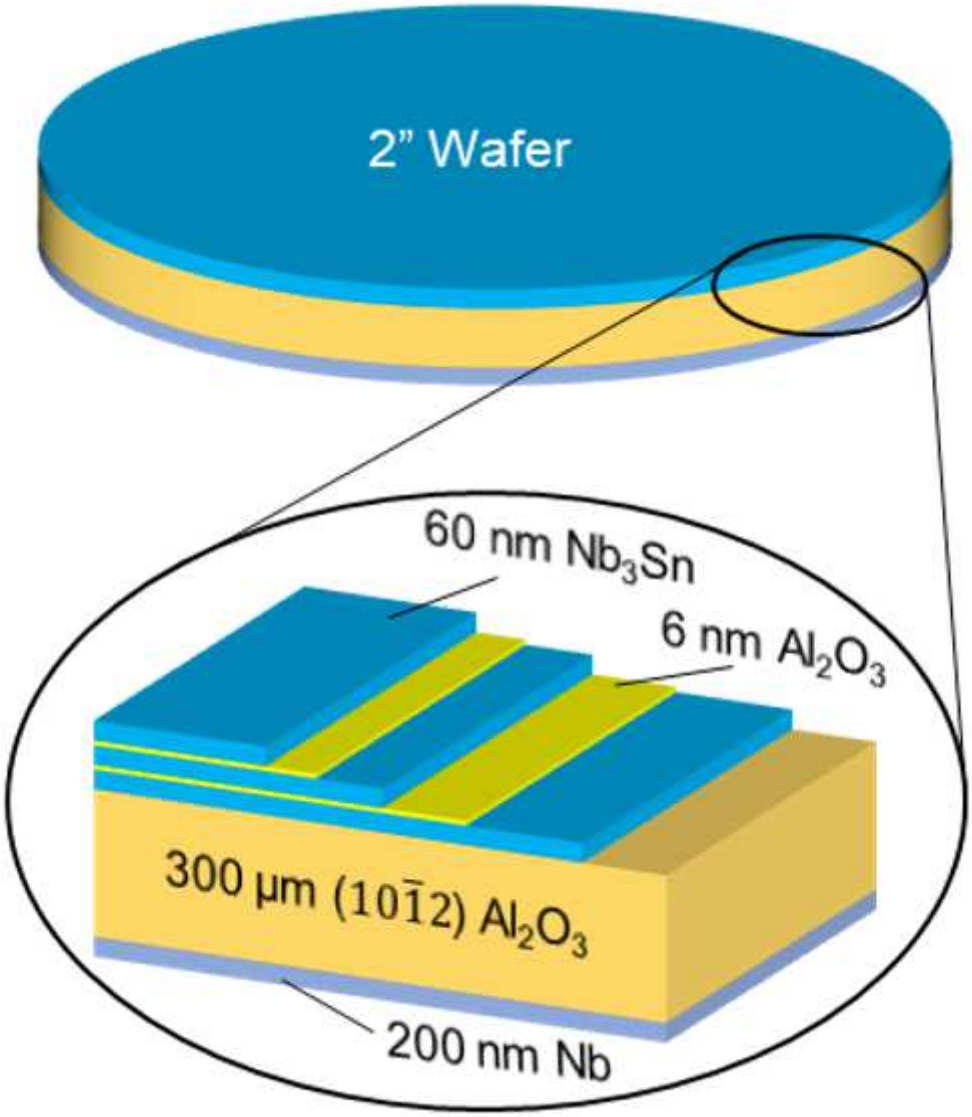

Figure 1

Schematic of Nb3Sn/Al2O3 multilayer heterostructures on Al2O3 wafer. Back side of Al2O3 wafer is coated with a thick Nb film.

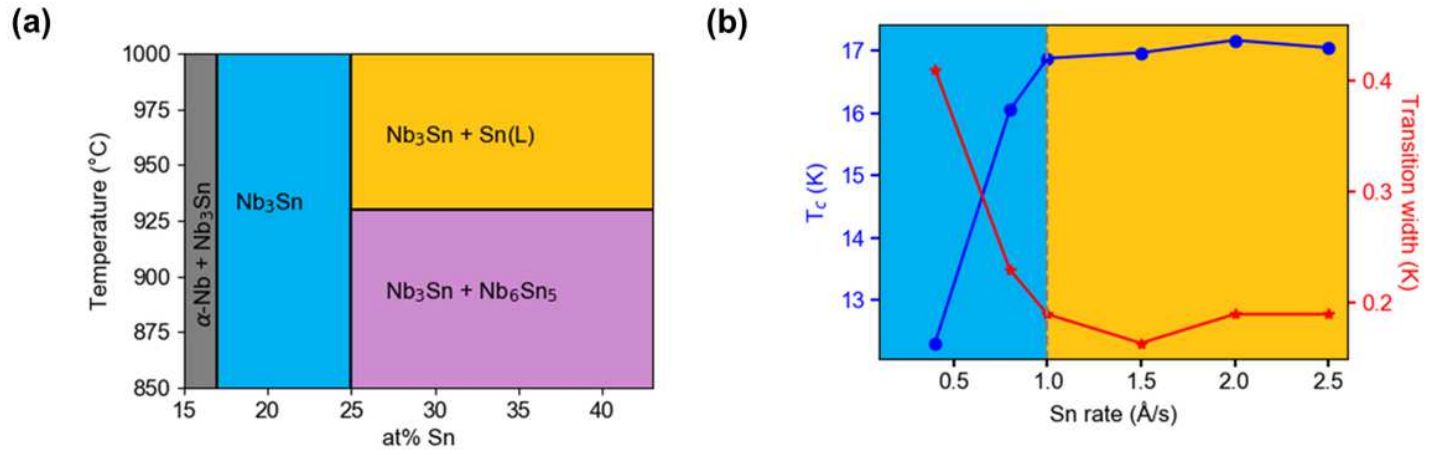

Figure 2

Connecting the Nb-Sn phase diagram to electrical properties and process window. (a) Relevant adsorption-controlled growth regime (orange) of Nb-Sn phase diagram. Nb3Sn spans 17-25 % Sn, and the desired Nb3Sn + liquid Sn field lies above 930 °C and 25% Sn. (b) Tc, ΔTc, vs the Sn flux of 60 nm thick Nb3Sn single layer thin films on Al2O3 substrates. Tc levels off above 1.0 Å/s Sn, corresponding to the adsorption-controlled growth window and the film composition reach 25% Sn.

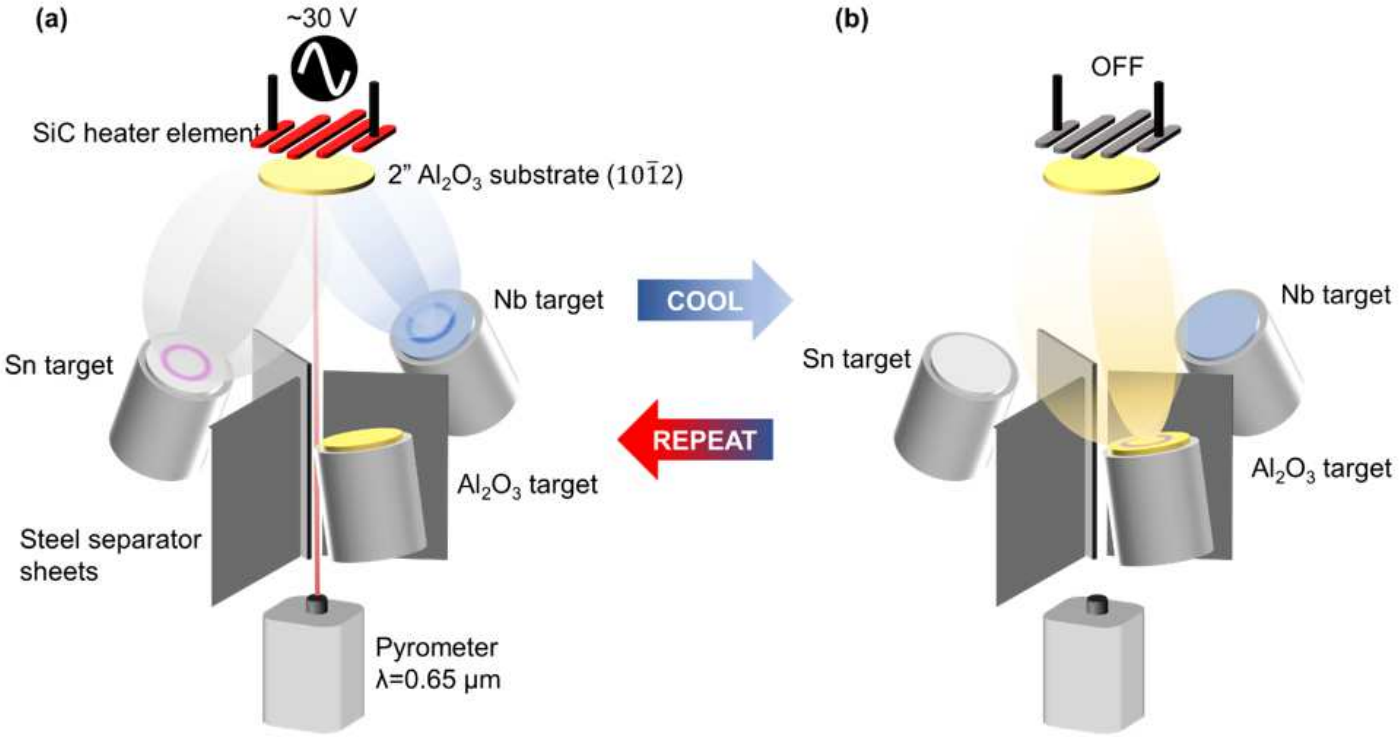

Figure 3

Schematic of thin films deposition setup and sequential processing steps for Nb3Sn/Al2O3 multilayer heterostructures. (a) Nb and Sn are sputtered onto Al2O3 substrate while heater element is powered on.

(b) After allowing film to cool, Al2O3 is sputtered from a single stoichiometric Al2O3 target. Sample is heated again to anneal Al2O3. These two steps are repeated to produce multilayer samples.

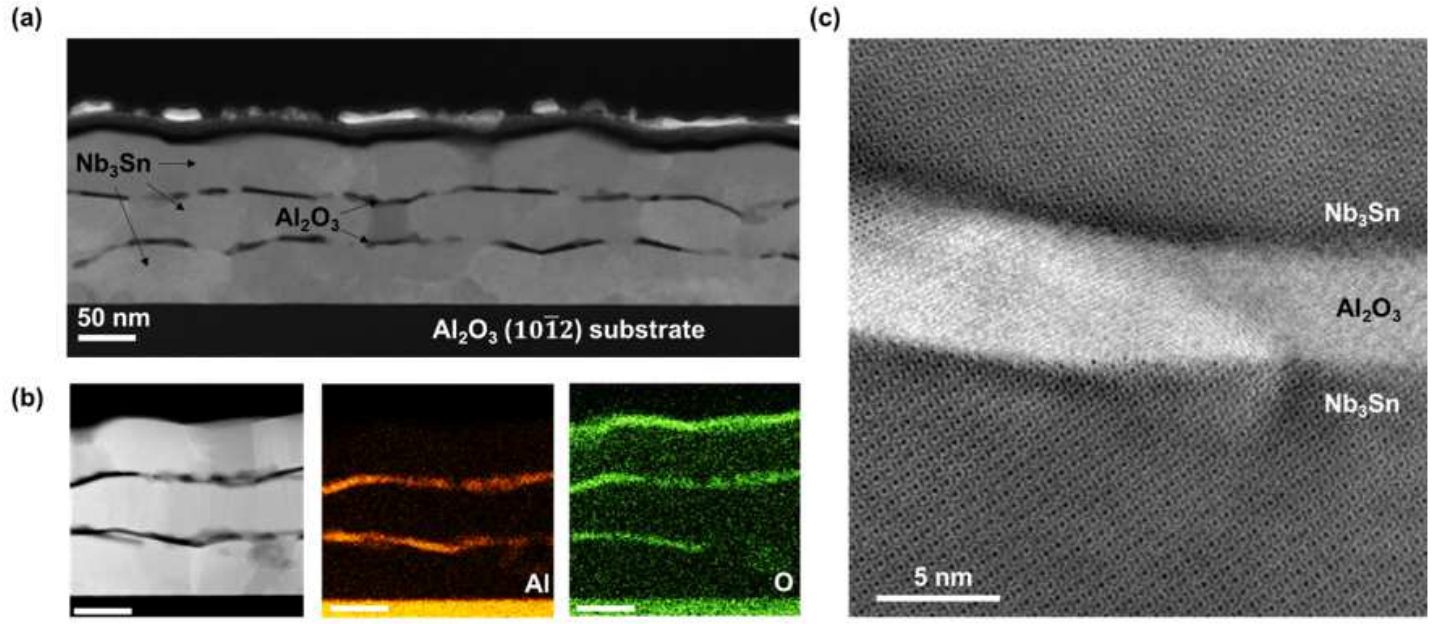

Figure 4

Cross-sectional transmission electron microscopy images of Nb3Sn/Al2O3 multilayer heterostructures (a) Low-magnification image of trilayer morphology. (b) EDS compositional mapping of Al and O showing no interdiffusion between Al2O3 and Nb3Sn. (c) High-magnification image of the interfaces between Al2O3 and Nb3Sn.

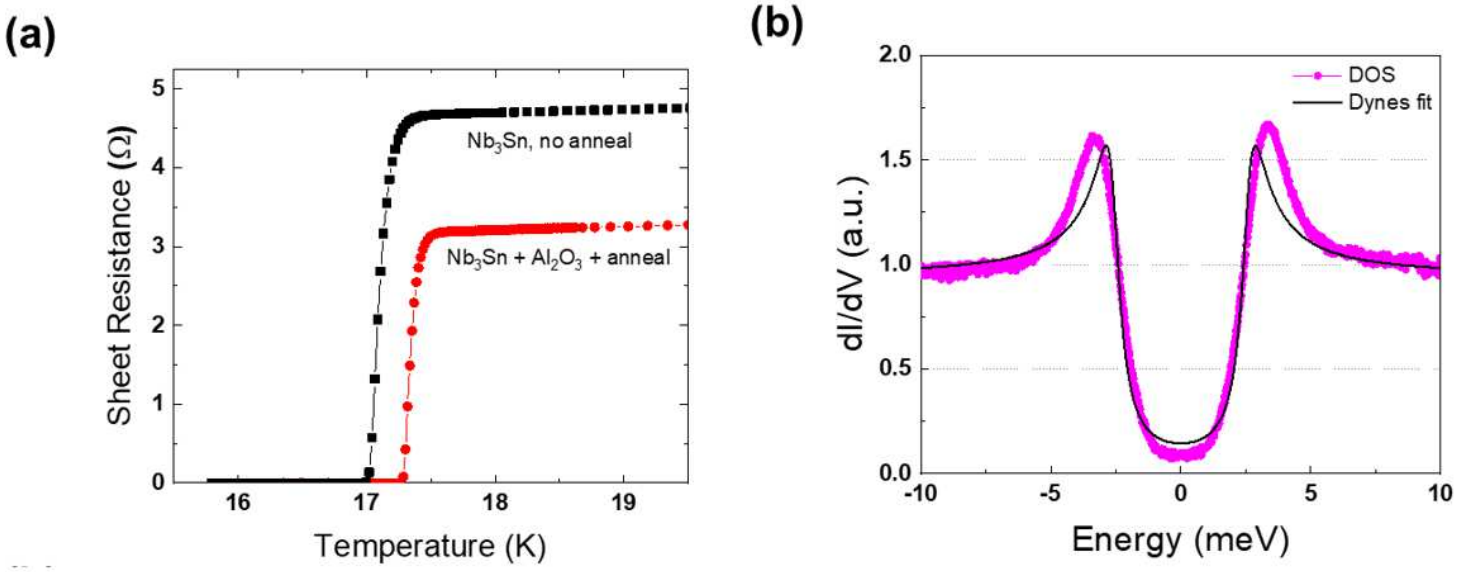

Figure 5

Electrical properties of single-layer Nb3Sn films. (a) Resistive superconducting transition for two identical 60 nm thick films, one of which is capped with 6 nm Al2O3 overlayer and annealed at 900 °C for 10 minutes. (b) Density of states measured by scanning tunneling microscopy and Dynes fit for a 60 nm thick Nb3Sn film.

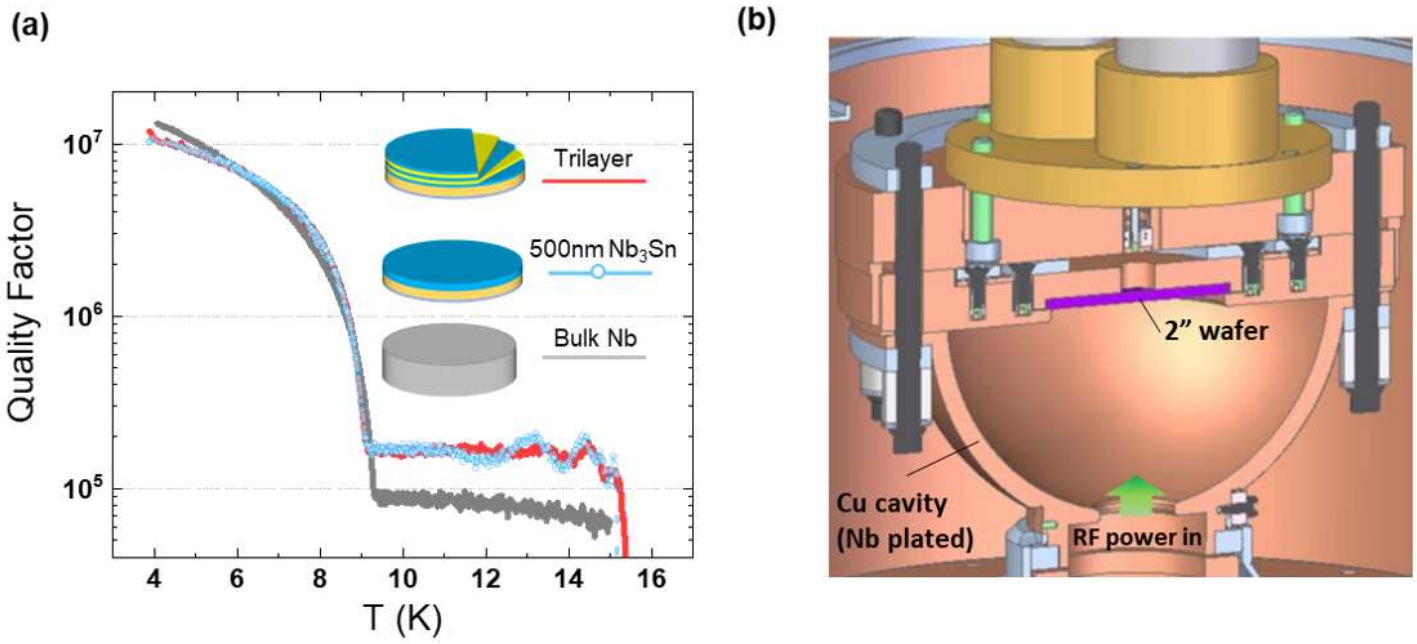

Figure 6

(a) RF Surface resistance measurements of Nb3Sn film and multilayer compared to cavity-grade Nb. (b) Cutaway of hemispherical resonator cavity at SLAC used for these measurements.

Supplementary Files

This is a list of supplementary files associated with this preprint. Click to download.

- Nb3SnmultilayerSupplementalInfoFinal.docx